Apparent fractality emerging from models of random distributions

Daniel Hamburger,[1,*] Ofer Biham,[1,†] and David Avnir[2,‡]
[1] *Racah Institute of Physics, The Hebrew University, Jerusalem 91904, Israel*
[2] *Institute of Chemistry, The Hebrew University, Jerusalem 91904, Israel*
(Received 24 October 1995)

The fractal properties of models of randomly placed n-dimensional spheres (n=1,2,3) are studied using standard techniques for calculating fractal dimensions in empirical data (the box counting and Minkowski-sausage techniques). Using analytical and numerical calculations it is shown that in the regime of low volume fraction occupied by the spheres, apparent fractal behavior is observed for a range of scales between physically relevant cutoffs. The width of this range, typically spanning between one and two orders of magnitude, is in very good agreement with the typical range observed in experimental measurements of fractals. The dimensions are not universal and depend on density. These observations are applicable to spatial, temporal, and spectral random structures. Polydispersivity in sphere radii and impenetrability of the spheres (resulting in short range correlations) are also introduced and are found to have little effect on the scaling properties. We thus propose that apparent fractal behavior observed experimentally over a limited range may often have its origin in underlying randomness.

PACS number(s): 64.60.Ak, 05.40.+j

I. INTRODUCTION

In recent years the study of fractal structures has been an active field of research both theoretically and experimentally [1–9]. In theory, a variety of algorithms and dynamical models that produce fractal sets have been introduced. Typically, in these models one can define an asymptotic limit in which the set exhibits fractal behavior on an arbitrarily broad range of length scales. One can then approach this limit by a process of gradual refinements of the set, which may involve either an increase in system size or a decrease in the minimal object size. In the case of *empirical fractals* observed experimentally the situation is different. For these fractals the range over which they obey a scaling law is restricted by inherent upper and lower cutoffs. In most experimental situations this range may be quite small, namely, not more than 1 or 2 orders of magnitude [10]. Nevertheless, even in these cases the fractal analysis condenses data into useful relations between different quantities and often provides useful insight [2–5].

Motivated by the yet largely inexplicable abundance of experimentally observed fractals, we consider in this paper the apparent fractal properties of systems that are governed by uniformly random distributions. The choice of random systems is justified by the abundance of randomness in nature, and by the fact that uniform randomness is a convenient limit, on top of which correlations can be introduced as perturbations. Although a purely random system cannot be fully scale invariant, it may, as we show below, display apparent fractality over a limited range. The width and the cutoff values of this range seem to be in good agreement with the typical width and typical cutoffs observed in experimental measurements (between one and two decades), unlike the case with models that are inherently scale free.

To illustrate these ideas we consider a model in which n-dimensional ($n = 1, 2, 3$) spheres of diameter d are randomly distributed in an n-dimensional space in the regime of low volume fraction occupied by the spheres. In three dimensions (3D) our definitions coincide with ordinary spheres, while for $n = 2$ (2D) we consider disks, and for $n = 1$ (1D) rods of length d. In the basic model the positions of the spheres are uncorrelated and they are thus allowed to overlap. We then extend the model to the case where there is a distribution of sphere radii and examine the effect of this distribution on the fractal properties. We also examine a version of the model in which spheres are not allowed to overlap, thus introducing short range correlations between sphere positions. This class of models may approximately describe spatial distribution of objects such as craters on the moon, droplets in a cloud, and adsorbates on a substrate. In particular, the one dimensional model may describe the level distribution in energy spectra of quantum systems and the zero set of random temporal signals. Therefore, such models may be at the root of empirical observations of fractals in experiments and data analyses, dealing with processes governed mainly by randomness [10]. As fractality is usually revealed by applying various resolution analyses, we also address the question of whether our observations are method dependent.

Two of the most commonly employed resolution analysis methods are the box-counting (BC) and Minkowski-sausage (MS) techniques [1,11]. The fractal properties

*URL: http://www.fh.huji.ac.il/~dani
†URL: http://www.fiz.huji.ac.il/staff_Acc/faculty/biham
‡Electronic address: david@granite.fh.huji.ac.il

of these models are studied here both analytically and numerically, within the BC and MS frameworks. The analytical solution is exact except for the case of impenetrable spheres in $n > 1$ dimensions where some approximations were needed.

In the box-counting procedure one covers the embedding space by nonoverlapping boxes of linear size r, and then counts the number of boxes $N(r)$ that have a nonempty intersection with the (fractal) set. A fractal dimension $D_{\rm BC}$ is declared to prevail at a certain range, if a relation of the type

$$N_{\rm BC}(r) \sim r^{-D_{\rm BC}} \tag{1}$$

holds, or equivalently, if the slope of the log-log plot

$$D_{\rm BC} = -\text{slope}\,\{\log_{10} r, \log_{10}[N_{\rm BC}(r)]\} \tag{2}$$

is found to be constant over that range. In the MS case [11] one draws an n-dimensional (n=1,2,3) Minkowski sphere (M sphere) of radius R around each point in the set under consideration, and calculates how the volume V of the union of all spheres changes under a variation of R. The set is considered fractal with a dimension $D_{\rm MS}$, over a range of scales, if

$$V(R) \sim R^{n-D_{\rm MS}}, \tag{3}$$

or equivalently, if

$$D_{\rm MS} = -\text{slope}\,\{\log_{10} R, \log_{10}[V(R)/R^n]\} \tag{4}$$

is constant within this range. The BC and MS methods are known to be identical from the mathematical point of view [11], where the limits $r, R \to 0$ can be taken. Their equivalence from the physical point of view, under the constraints of finite cutoffs, is not obvious. While it is clear from Eqs. (1)–(4) that both methods employ resolution analysis, in which the number of occupied "resolution units" (boxes or spheres) has to be determined as a function of the resolution magnitude (box length or M sphere radius), there are slight differences between the two methods, which are due to both geometrical differences and the presence of cutoffs.

Using a resolution analysis one should be aware of the existence of physical cutoffs. This is especially important in the structures considered below, which are not fractal in the rigorous mathematical sense. We will show that the log-log plots of the functions $N(r)$ and $V(R)$ display linear behavior between these physical cutoffs. The slope in this range can be interpreted as a fractal dimension (FD). The existence of this scaling behavior between physically relevant cutoffs is a central motivation for the study of the random models presented below.

The paper is organized as follows: in Sec. II we consider the basic model of penetrable spheres where all the spheres are of equal size, and calculate the BC function. From the analysis of this function we obtain the nontrivial linear range and extract the apparent FD. The generality of this model is then demonstrated using an information theory argument. In Sec. III we generalize the analysis to the case where the spheres are not equally sized but exhibit various size distributions and examine the effect on the apparent fractal behavior. Certain correlations are then introduced in Sec. IV where the case of impenetrable spheres in considered and the conclusions are given in Sec. V.

II. THE MODEL OF RANDOMLY DISTRIBUTED SPHERES

A. The 1D model

In this model M rods of length $d \ll 1$ are randomly placed on the unit interval (Fig. 1) [12] such that the

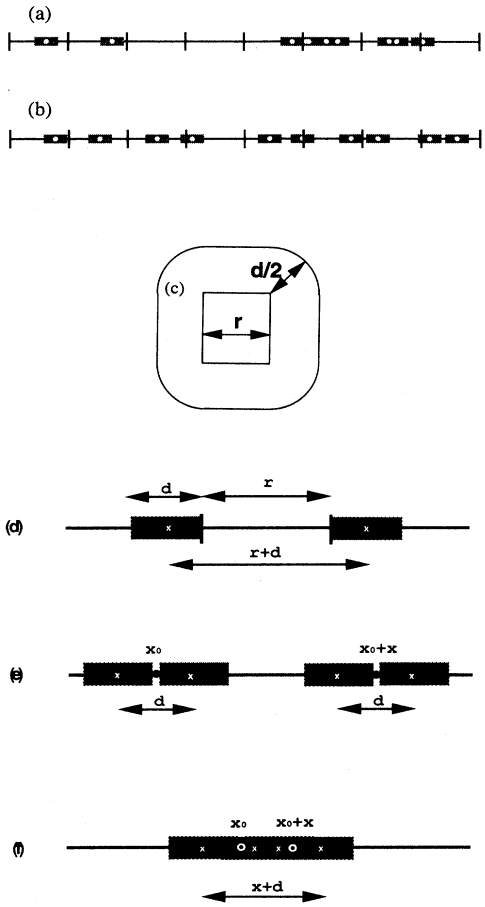

FIG. 1. Typical realizations of random placements of rods of size d (shaded with center dot) in the penetrable (a) and impenetrable (b) cases. Also shown is a division into "boxes" (vertical lines). The figure also represents the zero set of a temporal series of signals of width d, or a spectrum of randomly positioned energy levels with uncertainty width d. (c) Excluded area in the case of placement of disks in 2D. The excluded area consists of the box of side length r, four quarter circles of diameter d, and four rectangles rd. This is just the convolution of the box and a circle of diameter d. (d) Illustration of counting procedure used in our probabilistic arguments: For a box of length r to remain unintersected, no rod center may approach its ends closer than a distance of $d/2$. Hence a total length of $r + d$ must remain free. (e) Counting procedure in Sec. II D: Distance between the "test points" x is larger than d: for both points x_0 and $x_0 + x$ to be empty, a total length of $2d$ must be excluded. (f) If $x < d$, a rod falling in between the two points may overlap both, so a length of only $x + d$ is excluded.

positions of the rod centers are chosen from a uniform random distribution. The rods are mutually penetrable, namely, overlaps are allowed. The BC function $N(r)$ will now be derived. This function gives the number of boxes, for given box size r, which have a nonempty intersection with the set. For a large enough number of rods (of the order of 100 in the present case), the deviations from the expectation value $\langle N(r)\rangle$ are negligible and edge effects are unimportant. Let p denote the probability that a box of size r intersects a rod of length d. Then for a total of r^{-1} boxes,

$$\langle N(r)\rangle = \frac{p}{r}. \tag{5}$$

Following Refs. [13,14] define the probability q_1 that after random placement of the first rod, a given box remains unintersected. Neglecting edge effects, this implies that the center of the rod must be at least a distance of $d/2$ away from either edge of the box [Fig. 1(d)]. A total length of $r + 2(d/2)$ is, therefore, unavailable for placement without intersection. For a uniformly random distribution it follows that

$$q_1 = 1 - (r + d). \tag{6}$$

The next rods are placed independently, which means that after placement of M rods, the probability that the box is still unintersected is

$$q = [1 - (r + d)]^M. \tag{7}$$

Finally, the probability of at least one intersection is $p = 1 - q$, and therefore

$$\langle N(r)\rangle = \frac{1}{r}\left[1 - [1 - (r + d)]^M\right]. \tag{8}$$

This is the one dimensional BC function for randomly adsorbed, mutually penetrable rods [10]. Numerical simulations of the model along with the theoretical prediction of Eq. (8) are shown in Fig. 2. The excellent agreement is evident. The parameters d and M are independent, and are limited only by the restriction $\eta \leq 1$, where $\eta \equiv Md$ is the coverage of the line. We find that for large M (here $M > 100$) changing d and M while keeping η fixed, merely translates rigidly the BC function in the log-log plane.

In Fig. 3, the BC function is shown in a range between cutoffs, together with a linear regression. This is the range that is commonly measured in experimental work. The special significance of these cutoffs is discussed below. Notice the nearly linear appearance, extending over close to 1.5 decades.

B. Extension to 2D and 3D

In the two dimensional model one places *disks* of diameter d on the unit square, so that for a given box of area r^2 to remain unintersected, no disk center may fall within the area shown in Fig. 1(c). Thus, a total area of $r^2 + 4[\frac{1}{4}\pi\,(d/2)^2] + 4(r\,d/2)$ is excluded for placement of the first disk center. Therefore in this case the probability of the box to remain empty is

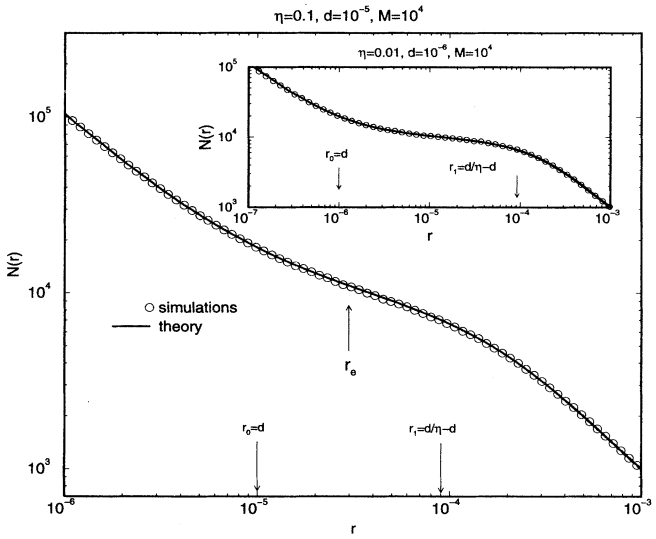

FIG. 2. Comparison of simulation results (circles) to the theoretical prediction of Eq. (8) (solid line) for the number of intersected boxes as a function of their size in the 1D penetrable rods case. The coverage is $\eta = 0.1$ and the rod length is $d/L = 10^{-5}$. The cutoffs are manifested as the two knees in the graph. The lower bound r_0 is seen to be indeed located at $r = d$. The upper bound r_1 is at $r = d/\eta - d$, also conforming with the prediction in the text. The agreement between theory and simulations is excellent over the entire range. Inset: Same with $\eta = 0.01$ and $d/L = 10^{-6}$. Note the increase in the range of linearity.

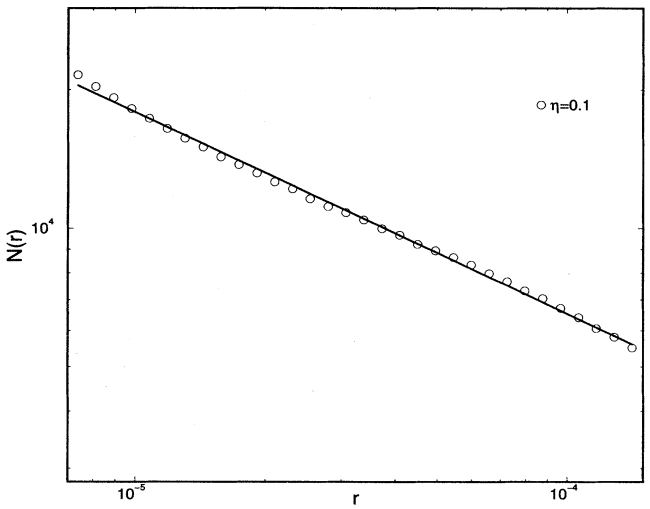

FIG. 3. The simulation results (circles) for the number of intersected boxes $N(r)$ vs r in the experimentally relevant range are shown along with a linear regression fit for coverage $\eta = 0.1$ (obtained for $d = 10^{-5}$, $N_d = 10^4$). This is the experimentally relevant range that is typically used to obtain the FD.

$$q_1 = 1 - \left(r^2 + \frac{1}{4}\pi d^2 + 2r\,d \right). \quad (9)$$

The next disks are placed independently, leading to

$$\langle N(r) \rangle = \frac{1}{r^2} \left\{ 1 - \left[1 - \left(r^2 + 2r\,d + \frac{1}{4}\pi d^2 \right) \right]^M \right\}. \quad (10)$$

Similarly, for 3D one considers independent placement of spheres, and the excluded volume for sphere centers is that formed by convolution of a cube of side r and a sphere of diameter d, which is $r^3 + 6(r^2\,d/2) + 12[r\,\frac{1}{4}\pi(d/2)^2] + 8[\frac{1}{8}\,\frac{4}{3}\pi\,(d/2)^3]$. One then obtains

$$q_1 = 1 - \left(r^3 + 3r^2\,d + \frac{3\pi}{4} r\,d^2 + \frac{\pi}{6} d^3 \right), \quad (11)$$

and

$$\langle N(r) \rangle = \frac{1}{r^3} \left\{ 1 - \left[1 - \left(r^3 + 3r^2\,d + \frac{3\pi}{4} r\,d^2 + \frac{\pi}{6} d^3 \right) \right]^M \right\}. \quad (12)$$

C. Cutoffs, range of linearity, and the fractal dimension

1. Cutoffs

We will now study the BC function $N(r)$ and examine the possibility of fractal-like behavior. For simplicity we will first concentrate on the 1D case, but the conclusions apply to 2D and 3D as well.

For mathematical fractals displaying full scale invariance, the log-log plot of $N(r)$ versus r can form a straight line with a fractal slope over an unlimited range of scales in the asymptotic limit. For the set we consider, this is clearly not the case as in Fig. 2: there are "knees" beyond which the slope approaches 1. This is due to the existence of lower and upper cutoffs, r_0 and r_1, respectively. These cutoffs correspond to relevant physical limits of observation. Here, the smallest feature is of size d, and so the finest resolution is of that size. No additional information is obtained by reducing r below $r_0 = d$, where D approaches the trivial limit of 1 as $r \to 0$. To see why this is so, suppose, for convenience, that the center of each rod is located at a point connecting two adjacent boxes: then halving the box doubles the number of intersected boxes if $r < d$, with the result that D must approach the limit of 1 as $r \to 0$. When the centers of the rods are located arbitrarily, the lower cutoff will not be sharply located at d. Nevertheless,

$$r_0 = d \quad (13)$$

is a good estimate for it. As for the upper cutoff r_1, it is the size beyond which practically all boxes intersect at least one rod, where again $D \to 1$. This happens when the boxes are larger than the average gap between rods:

$$r_1 = 1/M - d, \quad (14)$$

which is therefore an approximate upper cutoff. We thus have the approximate range $r_0 < r < r_1$, where the measurement is properly tuned to measure inherent scaling behavior, if it exists. For scaling behavior to be observed, there must be a minimal range of apparent linearity [Eq. (2)]. The size of such a range and the extent of linearity displayed by the BC function in it are considered below.

2. Range of linearity

The standard experimental procedure is to apply a linear regression analysis on the log-log presentation of the scaling range. The linear regression line is constructed to go through the inflection point $[r_i, N(r_i)]$ of the log-log plot of Eq. (8). The dependence of the range of linearity Δ on the coefficient of determination $\mathcal{R}^2$ (measuring the quality of the linear description) is then explored.

The range of linearity is approximately given by $\Delta = 2[\log_{10}(r_i) - \log_{10}(r_0)]$. Applying a linear regression analysis on the log-log plot of the BC function, we evaluated the slopes and actual ranges of linearity under these constraints, with different values of $\mathcal{R}^2$ imposed. Typical results are shown in Fig. 4. For instance, about two decades of linear behavior can be observed for a required value of $\mathcal{R}^2$ of below 0.97. Examples of experimentally observed fractal objects exhibiting several orders of magnitude of linearity are rare; the vast majority of reported fractality spans 1–2 orders of magnitude [2–8,10,15]. It is important to emphasize that, in fact, we are mimicking in our calculations the common practice of searching and reporting FD's in empirical data.

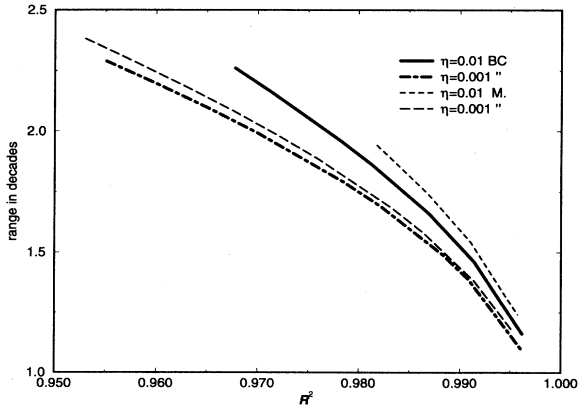

FIG. 4. The range of linearity Δ of Eq. (2), in a linear regression analysis. The range of linearity decreases as higher quality regression is required (see text). The results presented are valid in all dimensions, but it should be remembered that the same coverage corresponds to different interparticle distances in different dimensions.

The convention for the smallest meaningful scaling range is *one decade* [16]. Given this, a simple argument yields the maximum allowed coverage: By using the estimates above for the cutoffs, $r_0 = d$ and $r_1 = 1/M - d = d(1-\eta)/\eta$, one observes that a range $\Delta = \log_{10}(r_1) - \log_{10}(r_0) = \log_{10}[(1-\eta)/\eta]$ of at least one decade, requires that $\eta < 1/11$. It follows that the apparent fractality in our model is *restricted to* $\eta \leq 0.1$. The range between the cutoffs grows as the coverage is *decreased*, as observed in Fig. 2.

In addition to the width of the range between the cutoffs, the quality of the linear fit within this range, measured by $\mathcal{R}^2$ should also be considered. One can limit the range of linearity by imposing a lower bound on $\mathcal{R}^2$: obviously, the range decreases as $\mathcal{R}^2$ increases (Fig. 4). Also note from this figure that for a given range the quality of linearity grows as the coverage is *increased*, or as the slope of the BC function between the cutoffs (i.e., the FD) approaches 1 (Fig. 2). This happens because of the smooth merging with the slope beyond the cutoffs, which is trivially 1. We thus conclude that the two cutoffs limit the width of the linear range for high coverage while the $\mathcal{R}^2$ criterion limits it for low coverage. As a result, the range of scales in which we observe apparent fractality is typically between one and two orders of magnitude.

3. *Fractal dimension*

The apparent FD shown in Fig. 5, for an imposed value of $\mathcal{R}^2 = 0.995$, rises monotonically from 0 as more rods are added. This is an important aspect of the model: it does not predict a universal (specific) FD, but the whole allowable range of FD values. The regression results are further compared in Fig. 5 to an analytical equation, obtained by calculating the logarithmic derivative of $N(r)$ at the *estimated* middle point $r_e = \sqrt{r_0 r_1}$:

$$D_{\mathrm{BC}}^{(1)} = \left.\frac{d(\log_{10}[N(r)])}{d(\log_{10}[1/r])}\right|_{r=r_e}$$

$$= 1 - \sqrt{\eta(1-\eta)}\,\frac{\left\{1-[\eta+\sqrt{\eta(1-\eta)}]/M\right\}^{M-1}}{1-\left\{1-[\eta+\sqrt{\eta(1-\eta)}]/M\right\}^{M}}. \tag{15}$$

We use an estimate for the middle point (r_e) rather than the exact result (r_i), since r_i cannot be given analytically. The almost symmetric S shape of the log-log plot in the scaling region assures that r_e is a good estimate for r_i. As seen in Fig. 5, the FD predicted by Eq. (15) is an accurate lower bound to the regression result.

By using $(1+x/N)^N \to e^x$ as $N \to \infty$, Eq. (15) may be simplified in the "thermodynamic limit," while keeping η finite. One then obtains

$$D_{\mathrm{BC}}^{(1)} = 1 - \frac{\sqrt{\eta(1-\eta)}}{\exp\left[\eta+\sqrt{\eta(1-\eta)}\right]-1}. \tag{16}$$

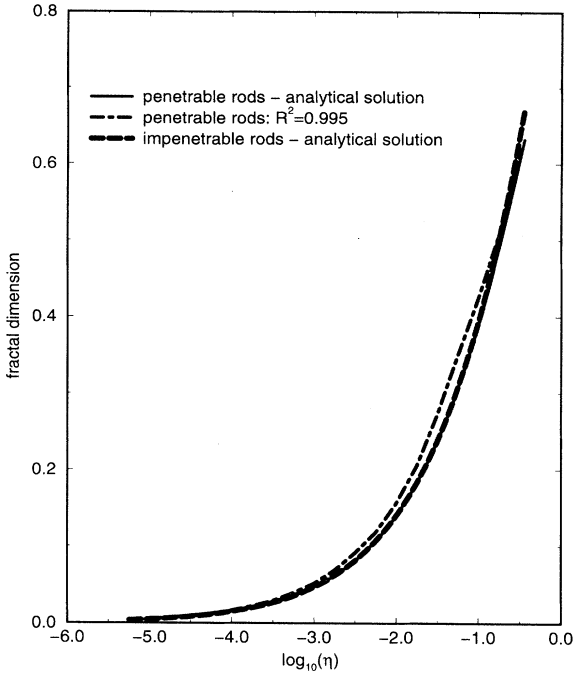

FIG. 5. Apparent fractality (FD) as computed by linear regression with a relatively high (0.995) coefficient of determination, in the case of rods. The predictions of the analytical equations, Eqs. (15) and (65), serve as accurate lower bounds. The prediction for the FD of the penetrable and impenetrable rods cases is seen to differ only marginally, indicating that the dominant contribution to the FD comes from the penetrable (i.e., totally random) rods case. The lowest coverage shown corresponds to the lowest molecular densities observed in nature: 10 cm^{-3} in intergalactic space.

Notably, the expression for $D_{\mathrm{BC}}^{(1)}$ depends on η alone. In the limit of small η, one can further simplify Eq. (16) and obtain

$$D_{\mathrm{BC}}^{(1)} \approx \left(\frac{\eta}{1-\eta}\right)^{1/2}, \qquad \eta \ll 1. \tag{17}$$

Expressions for $D_{\mathrm{BC}}^{(2)}$ and $D_{\mathrm{BC}}^{(3)}$ may be derived from Eqs. (10) and (12) for the 2D and 3D cases. These, as well as a discussion of their cutoffs and range of linearity, are deferred to Sec. III A 2, where a more general model is treated.

D. Absence of correlations

Since fractal objects typically exhibit some correlations, one might wonder whether the finding of an apparent FD in our model is also due to some hidden correlations within a certain window of resolution. For instance, it might seem plausible that the finite extent of the rods introduces a correlation, for if a point on the line belongs to a certain rod, then a point at a distance $x < d$ is likely to belong to the same rod. However, correlations at a

scale $x < d$ below the lower cutoff are, rightly so, typically not measured. Furthermore, as we show next, the correlation exponent for $x > d$ vanishes. This will prove that the emergence of an FD in the penetrable rods case is *not* due to the presence of correlations, but entirely due to the scaling displayed by the underlying uniform distribution.

A correlation exponent ν is associated with a given set if a correlation function $c(x)$ has the following power-law form over a sufficiently large range:

$$c(x) \sim x^{-\nu}. \tag{18}$$

An exact expression for this function may be derived for penetrable rods. Let $\theta(x_0)$ be the local density at the point x_0 on the line. That is, $\theta(x_0) = 1$ if x_0 belongs to a rod, and zero otherwise. The correlation function is defined as

$$c(x) = \langle \theta(x_0)\, \theta(x_0 + x) \rangle, \tag{19}$$

where $\langle\ \rangle$ denotes either an ensemble average (at fixed x_0), or an average over x_0. Assuming ergodicity, we choose to calculate the latter. Only pairs of points $(x_0, x_0 + x)$ such that both $\theta(x_0)$ and $\theta(x_0+x)$ are 1 contribute to the average. We thus require the simultaneous probability:

$$P(x, x_0) \equiv \Pr\left[(\theta(x_0 + x) = 1) \cap (\theta(x_0) = 1)\right]. \tag{20}$$

The correlation function is then

$$c(x) = \int_0^1 dx_0\, \theta(x_0)\, \theta(x_0 + x)\, P(x, x_0), \tag{21}$$

where one can set $\theta(x_0) = \theta(x_0 + x) = 1$. Neglecting edge effects, $P(x, x_0)$ does not depend on x_0, since we are considering a statistically homogeneous medium (or stationary process). In what follows, therefore, x_0 is considered to be any convenient reference point, though none of the results depends on its location. With this general choice of x_0, one obtains from Eq. (21):

$$c(x) = P_{x_0}(x) = \Pr\left[(\theta(x_0 + x) = 1) \cap (\theta(x_0) = 1)\right]. \tag{22}$$

To evaluate $P_{x_0}(x)$, consider a modification of the argument that led to Eq. (7) : pick two "test points" at random on a line of length L and denote their respective positions x_0 and $x_0 + x$. Now consider randomly placing rods of length d on the line. The events that are complementary to *both* points (x_0, x_0+x) being occupied are (1) that at least one is unoccupied (with probability Q_1), and (2) that both are unoccupied $[Q_2(x)]$. Clearly Q_1 already accounts for $Q_2(x)$, so that

$$P_{x_0}(x) = 1 - [2Q_1 - Q_2(x)]. \tag{23}$$

The evaluation of Q_1 is a repetition of the argument leading to Eq. (7), with a vanishing box size ($r = 0$). Thus,

$$Q_1 = (1 - d)^M \to e^{-\eta} \tag{24}$$

when $M \to \infty$. $Q_2(x)$ requires that no rod center is placed within a distance smaller than $d/2$ to either test point [see Figs. 1(e),(f)]. When $x > d$, this clearly excludes a total length of $2d$ from possible placement of rod centers. When $x < d$, a length of only $x + d$ is excluded, due to overlap of the two inner segments. In all other respects the argument leading to Eq. (7) (with $r = 0$) is again repeated, so that

$$Q_2(x) = \{1 - [d + s(x)]\}^M \to e^{-\rho[d+s(x)]}, \tag{25}$$

where $\rho^{-1} = 1/M$ is the average distance between rod centers, and

$$s(x) = \begin{cases} d, & x \geq d, \\ x, & x < d. \end{cases} \tag{26}$$

Combining Eqs. (22)–(26), one finally obtains for the correlation function:

$$c(x) = \begin{cases} 1 - 2e^{-\eta} + e^{-2\eta}, & x \geq d \\ 1 - 2e^{-\eta} + e^{-\eta} e^{-\rho x}, & x < d. \end{cases} \tag{27}$$

Thus for $x \geq d$, $c(x)$ is constant, i.e., *the correlation exponent vanishes* (a result obtained numerically by Meakin and Deutch [17]). However, the nontrivial range of the similarity dimension *starts* at d, and hence cannot possibly be due to correlations. These exist, not surprisingly, for $x < d$, but even there they decay *exponentially* (with a characteristic length of $1/M$), and not as a power law, as required for fractality measured by the scaling of correlation functions.

This completes the demonstration that the nontrivial result we obtained for the similarity dimension of penetrable rods is *not* due to correlations. The elements of this demonstration are applicable also to the more general model presented in the next section and are not repeated there: the absence of correlations holds for all penetrable cases treated in this study.

E. Generality of the model

In this section arguments are presented showing that the model of randomly placed, mutually penetrable spheres introduced in Sec. II is very general in the sense that it is a prototype of a much larger family of random processes. Being minimalistic in assumptions, the model is in fact a *generic* one for random processes. An information-theoretical approach is now employed to show this, using the fact that the only assumption entering the model is the *knowledge of a mean quantity.* An important feature of the information-theoretical approach is that it extends the model from spatial to *temporal* random sequences, and even to energy-level distributions [18]. Thus, in an adsorption process the relevant mean quantity is the average density of adsorbates and one seeks the distribution of nearest-neighbor distances. An equivalent situation is that in which one knows the average period of a time signal and is interested in the distribution of intervals between successive crossings of the time axis (the "zero set"). A finite width d is then the signal width at the crossings. Yet another case is that of spectral-level distribution (where d is the uncertainty bandwidth), for which it is well known that spacings of quantum energy levels in classically nonchaotic

systems are exponentially distributed [19]. Indeed, it will be shown that an exponential distribution of the intervals between the centers of the spheres is an inherent characteristic of our model. It shall then become clear that spatial, temporal, and spectral random processes fall into the same class. The spatial and temporal cases differ only in that a time process must be *ordered* on the time axis, while the positions of "events" on a spatial axis are not necessarily ordered. There are, however, $N!$ possible arrangements in the spatial case, obtained by interchanging the labels of events on the spatial axis. The time process may be considered as the one ordered set out of all these permutations. Relabeling is all that is required to map a spatial process to one in time, and clearly this does not affect the statistics of positions or intervals. Furthermore, it is well known [1] that the FD of the actual time signal can be deduced from that of its zero set. Relying on the equivalence just discussed, we choose in what follows for concreteness to work on the spatial process of placement, but one should keep in mind that the discussion applies just as well to time processes and energy-level spacings.

1. *Information-theory argument*

Consider now the derivation of the distribution satisfying the assumption of knowledge of the mean. In the present case this is the known average placement density

$$\langle x \rangle = \frac{M}{L} \tag{28}$$

(or equivalently, this may represent the average period of a time signal.) The arguments presented here for 1D are again easily generalized to 2D and 3D. Following a standard information-theory argument [20], the resulting distribution $P(x)$ of distances x between neighboring adsorbate centers is obtained by maximizing the missing information S,

$$S = -\int_0^\infty P(x)\,\ln P(x)\,dx, \tag{29}$$

where the constraint of knowing $\langle x \rangle$ can be written as

$$\langle x \rangle = \int_0^\infty x\,P(x)\,dx. \tag{30}$$

To this one must add the normalization constraint

$$\int_0^\infty dx\,P(x) = 1. \tag{31}$$

Using Lagrange multipliers λ and μ, the maximization of S can then be written in terms of a functional F as

$$F[P(x)] = -\int_0^\infty dx\,\{P(x)\,\ln P(x) + \lambda\,P(x) + \mu\,x\,P(x)\}, \tag{32}$$

whose variational derivative is

$$\delta F = -\int_0^\infty dx\,\{\ln P + 1 + \lambda + \mu\,x\}\delta P. \tag{33}$$

The arbitrariness of δP then requires the vanishing of the term in curly brackets, or

$$P(x) = e^{-(1+\lambda)}e^{-\mu x}. \tag{34}$$

Inserting this into the constraint equations, Eqs. (30) and (31), yields the distribution of nearest-neighbor distances

$$P(x) = \frac{1}{\langle x \rangle}\,e^{-x/\langle x \rangle}. \tag{35}$$

The appearance of an exponential distribution is not surprising: it is the Maxwell distribution when the average energy is given as the constraint in the canonical ensemble, or it shows up as the distribution of time intervals between successive radioactive decays, where the mean lifetime acts as the known constraint. It remains to be shown, returning to the adsorption language, that given this exponential distribution of intervals between the centers of the rods, the adsorbate *positions* are *uniformly* distributed.

2. *The position distribution*

It is a standard exercise in probability theory to show that a uniform distribution of positions leads to an exponential distribution of intervals (see, e.g., Ref. [21], or recall the argument for the time of flight of a particle undergoing random collisions with a given mean free path). It is now shown that the opposite holds as well, namely, that the exponential distribution of intervals, derived above from an information-theory argument, leads to a uniform distribution of positions. The argument that led to the derivation of the exponential distribution of intervals, Eq. (35), assumed that only the mean distance between points is known, and that this is the only parameter of relevance. Therefore, it was in fact implicitly assumed that successive placements are independent (for otherwise additional constraints should have appeared, reflecting the dependence of the distribution of intervals on the number of previous placements). Let $P(x)$ denote the probability density of finding a point between x and $x + dx$ after a single placement. Given that there is a point at x_0, consider the conditional probability density $g(x_0 + x|x_0)$ of finding the nearest-neighboring point between $x_0 + x, x_0 + x + dx$. This can be expressed as

$$g(x_0 + x|x_0) = \frac{1}{\langle x \rangle}\,e^{-x/\langle x \rangle}P(x_0 + x)dx, \tag{36}$$

where $\exp(-x/\langle x \rangle)/\langle x \rangle$ is the probability density of finding a gap of length x. But since this exponential probability depends only on the (non-negative) *distance* between neighboring points, it is clear that nothing prevents interchanging the roles of x_0 and $x_0 + x$; i.e. it must hold that

$$g(x_0 + x|x_0) = g(x_0|x_0 + x), \tag{37}$$

or, explicitly,

$$\frac{1}{\langle x\rangle}\, e^{-x/\langle x\rangle} P(x_0+x)dx = \frac{1}{\langle x\rangle}\, e^{-x/\langle x\rangle} P(x_0)dx_0. \quad (38)$$

One is at liberty to choose $dx = dx_0$, so that $P(x_0) = P(x_0+x)$, which holds for every x. Therefore $P(x)$ is *constant*, i.e., the positions are uniformly distributed. This result followed from the exponential distribution that was derived under the minimalistic assumption of knowledge of the mean of a relevant property. Drawing on the generality of this derivation, we conclude that *a uniform random distribution of adsorbate centers is a generic model of random processes in space and time*, where one only assumes knowledge of the mean. A uniform distribution of adsorbate centers is, however, exactly what was assumed in the adsorption model in Sec. II, for which apparent fractality was detected. Fractality may therefore be expected for any other random system that can be characterized by its mean.

One may further employ the above information-theory formalism in order to derive the distributions appropriate to knowledge of higher moments, if correlations are present in the system.

III. POLYDISPERSED MUTUALLY PENETRABLE SPHERES

A. The model

The basic model introduced in Sec. II is now generalized, by allowing polydispersivity in radii. That is, we consider a model of randomly placed n-dimensional spheres with a *distribution of radii* $P(a)$. The radii are assumed to be chosen independently from $P(a)$. In 1D, this may, e.g., represent a random spectrum with levels exhibiting a distribution of lifetimes. In 2D, such systems may approximately describe, for example, the formation of metal clusters on metal surfaces [22–24]. In 3D one might consider the distribution of atmospheric or intergalactic dust aggregates. Thus the polydispersed case represents a very wide class of systems, whose possible scaling properties and apparent FD are quantities of interest. Both the BC and MS functions and FD's will be calculated, first generally, and then for a number of specific but broadly used radii distributions.

1. Minkowski analysis

The Minkowski function and dimension corresponding to the model of polydispersed spheres introduced above, is calculated next.

a. The Minkowski function. Let all lengths be normalized to the total linear extent of the surface L. For a given probability distribution of radii $P(a)$, consider the determination of the MS function for M randomly placed spheres with a specific realization of radii out of $P(a)$, $\mathbf{a} \equiv (a_1, a_2, ..., a_M)$. The MS function for this realization, $V_{\mathbf{a}}^{(n)}(R)$, is the volume of the union of spheres of radius R centered at all points in the set under consideration. This amounts to increasing the intrinsic radius of a sphere a_i to $a_i + R$, and then calculating the volume of the union. Let the total volume of the embedding space be V_t. It is convenient to work with the normalized volume $\alpha_{\mathbf{a}}^{(n)}(R) \equiv V_{\mathbf{a}}^{(n)}(R)/V_t$. The calculation of $\alpha_{\mathbf{a}}^{(n)}(R)$ is very similar to the calculation of the BC function. A point is randomly chosen in the embedding space, and one calculates the probability q_M that after placement of M spheres with radii $\mathbf{a}$, the chosen point is not included in the volume of any of the spheres. The probability q_1 for this to happen after random placement of the first sphere is proportional to the volume remaining after subtracting the volume of this sphere,

$$q_1 = 1 - \frac{\gamma_n (a_1+R)^n}{V_t}, \quad (39)$$

where

$$\gamma_n = \begin{cases} 2, & n=1 \\ \pi, & n=2 \\ 4\pi/3, & n=3 \end{cases} \quad (40)$$

is a geometrical factor associated with the volume of an n-dimensional sphere. The next placements are independent, so that

$$q_M = \prod_{i=1}^{M} \left(1 - \frac{\gamma_n (a_i+R)^n}{V_t}\right). \quad (41)$$

Now, $1-q_M$ is the probability of finding the chosen point *in* the set, which on the other hand is equal to the normalized volume of the set. Thus,

$$\alpha_{\mathbf{a}}^{(n)}(R) = 1 - \prod_{i=1}^{M} \left(1 - \frac{\rho\,\gamma_n (a_i+R)^n}{M}\right), \quad (42)$$

where $\rho = M/V_t$ is the number density.

Next, one averages over all possible realizations of radii. Let

$$\langle f(a)\rangle \equiv \int P(a)\, f(a)\, da \quad (43)$$

denote the average of any function of the radius. Then the expectation value of the normalized volume, when each realization of radii $\mathbf{a}$ is weighted by its probability $\prod_{i=1}^{M} P(a_i)\, da_i$, is given by

$$\alpha^{(n)}(R) \equiv \langle \alpha_{\mathbf{a}}^{(n)}(R)\rangle = 1 - \int \prod_{i=1}^{M} da_i\, P(a_i) \left(1 - \frac{\rho\,\gamma_n (a_i+R)^n}{M}\right)$$
$$= 1 - \left[\int da\, P(a) \left(1 - \frac{\rho\,\gamma_n (a+R)^n}{M}\right)\right]^M = 1 - \left(1 - \frac{\rho\,\gamma_n \langle (a+R)^n\rangle}{M}\right)^M. \quad (44)$$

In the limit of large M one finally obtains

$$\alpha^{(n)}(R) = 1 - e^{-\rho\gamma_n\langle(a+R)^n\rangle}, \tag{45}$$

and, explicitly for each dimension:

$$\begin{aligned}
\alpha^{(1)}(R) &= 1 - \exp\left[-2\rho(R + \langle a\rangle)\right], \\
\alpha^{(2)}(R) &= 1 - \exp\left[-\pi\rho(R^2 + 2R\langle a\rangle + \langle a^2\rangle)\right], \\
\alpha^{(3)}(R) &= 1 - \exp\left[-\frac{4\pi}{3}\rho(R^3 + 3R^2\langle a\rangle + 3R\langle a^2\rangle + \langle a^3\rangle)\right].
\end{aligned} \tag{46}$$

b. The fractal dimension. To find the FD according to Eq. (4), we evaluate the logarithmic derivative of $\alpha^{(n)}(R)$, which is found to be

$$\frac{d\log_{10}\left(\alpha^{(n)}(R)/R^n\right)}{d\log_{10}(1/R)} = n - \frac{\rho\gamma_n\left(\sum_{k=1}^{n} k\,R^k\langle a^{n-k}\rangle\right)\exp\left[-\rho\gamma_n\langle(a+R)^n\rangle\right]}{1 - \exp\left[-\rho\gamma_n\langle(a+R)^n\rangle\right]}. \tag{47}$$

In analogy with the discussion in Sec. II C, one may expect the cutoffs to be found approximately at

$$R_0 = \langle a\rangle \quad \text{and} \quad R_1 = \tfrac{1}{2}\rho^{-1/n} - \langle a\rangle, \tag{48}$$

compared to $r_0 = d$ and $r_1 = \rho^{-1/n} - d$ for BC. The difference from BC by a factor of 2 is due to the appearance of *radii* as opposed to box lengths (which are equivalent to diameters). As in Sec. II C 2, we define the FD to be the slope at the estimated middle point $R_e = \sqrt{R_0 R_1}$ of the scaling range,

$$D_{\mathrm{MS}}^{(n)} = \left.\frac{d\log_{10}\Phi\log_{10}(\alpha^{(n)}(R)/R^n)}{d\log_{10}(1/R)}\right|_{R=R_e}, \tag{49}$$

which yields

$$\begin{aligned}
D_{\mathrm{MS}}^{(1)} &= 1 - \frac{\sqrt{\eta_1(1-\eta_1)}}{\exp\left[\eta_1 + \sqrt{\eta_1(1-\eta_1)}\right] - 1} = 1 - \frac{\nu_1^{1/2}\phi_1^{1/2}}{\exp\left(\eta_1 + \nu_1^{1/2}\phi_1^{1/2}\right) - 1} \\
D_{\mathrm{MS}}^{(2)} &= 2 - \frac{\nu_2^{3/4}\phi_2^{1/2} + 2\nu_2^{1/2}\phi_2}{\exp\left(\eta_2 + \nu_2^{3/4}\phi_2^{1/2} + \nu_2^{1/2}\phi_2\right) - 1}, \\
D_{\mathrm{MS}}^{(3)} &= 3 - \frac{(\lambda^{2/3}\mu - (2\mu)^2)^{1/2} + 2\nu_3^{2/3}\phi_3 + 3\nu_3^{1/2}\phi_3^{3/2}}{\exp\left(\eta_3 + (\lambda^{2/3}\mu - (2\mu)^2)^{1/2} + \nu_3^{2/3}\phi_3 + \nu_3^{1/2}\phi_3^{3/2}\right) - 1},
\end{aligned} \tag{50}$$

where for convenience a number of parameters are defined as follows:

$$\begin{aligned}
\eta_n &= \rho\gamma_n\langle a^n\rangle, \\
\nu_n &= \eta_n\frac{\langle a\rangle^n}{\langle a^n\rangle}, \\
\phi_n &= \tfrac{1}{2}\gamma_n^{1/n} - \nu_n^{1/n}, \\
\mu &= \tfrac{3}{2}\eta_3\frac{\langle a^2\rangle\langle a\rangle}{\langle a^3\rangle}, \\
\lambda &= \eta_3\frac{(\pi\langle a^2\rangle)^{3/2}}{\gamma_3\langle a^3\rangle}.
\end{aligned} \tag{51}$$

The parameter η_n is simply the *coverage* [25]; the other parameters measure various moments of the radius distribution.

The expressions for $D_{\mathrm{MS}}^{(n)}$ can be simplified somewhat for the case of a constant radius, whence $\langle a^n\rangle = a^n$, and consequently $\eta_n = \nu_n$. Note that the FD contains useful information about the first n moments of the radius distribution. In the next section the BC function of the same model of polydispersed radii is solved for, in order to compare the MS and BC methods.

2. Box-counting analysis

a. The BC function. Once again, take all lengths to be normalized to the total linear extent of the surface L. Repeating the averaging arguments used to arrive at Eq. (44), combined with the derivations of Eqs. (8), (10), and (12), leads to the following result for the BC (density) function in the polydispersed case:

$$\begin{aligned}
N^{(n)}(r) &\equiv \langle N_{\mathbf{a}}^{(n)}(r)\rangle \\
&= \frac{1}{r^n}\left[1 - \left(1 - \frac{\rho}{M}\sum_{k=0}^{n}\beta_{kn}\,r^k\,\langle a^{n-k}\rangle\right)^M\right].
\end{aligned} \tag{52}$$

Here r is the normalized box length, $\rho = M/V_t$ is the number density, and

$$\beta_{kn} = \begin{cases} \gamma_n, & k = 0 \\ 1, & k = n \\ 2n, & k = n-1 \\ 3\pi, & k = 1,\ n = 3 \end{cases} \tag{53}$$

is introduced for convenience. Taking the limit of large M, one finds

$$N^{(n)}(r) = \frac{1}{r^n}\left[1 - \exp\left(-\rho \sum_{k=0}^{n} \beta_{kn}\, r^k\, \langle a^{n-k}\rangle\right)\right]. \tag{54}$$

Although at first sight this result may seem to differ substantially from that for the MS function $\alpha^{(n)}(R)$ [Eq. (45)], the two will be compared in Sec. III B 2 and shown to be quite similar.

b. The fractal dimension. Proceeding with the calculation of the FD, evaluation of the logarithmic derivative yields

$$\frac{d\log_{10}(N^{(n)}(r))}{d\log_{10}(1/r)} = n - \frac{\rho\left(\sum_{k=1}^{n} k\,\beta_{kn}\, r^k \langle a^{n-k}\rangle\right)}{\exp\left(\rho \sum_{k=0}^{n} \beta_{kn}\, r^k \langle a^{n-k}\rangle\right) - 1}. \tag{55}$$

As usual, the FD is defined as the slope at the estimated middle point $r_e = \sqrt{r_0\, r_1}$ between the lower and upper cutoffs, $r_0 = 2\langle a\rangle$ and $r_1 = \rho^{-1/n} - 2\langle a\rangle$:

$$D_{\rm BC}^{(n)} = \left.\frac{d\log_{10}(N^{(n)}(r))}{d\log_{10}(1/r)}\right|_{r=r_e}, \tag{56}$$

with the result

$$\begin{aligned}
D_{\rm BC}^{(1)} &= 1 - \frac{\sqrt{\eta_1(1-\eta_1)}}{\exp\left[\eta_1 + \sqrt{\eta_1(1-\eta_1)}\right] - 1} = 1 - \frac{\zeta_1^{1/2}\,\psi_1^{1/2}}{\exp\left(\eta_1 + \zeta_1^{1/2}\,\psi_1^{1/2}\right) - 1}, \\
D_{\rm BC}^{(2)} &= 2 - \frac{\zeta_2^{3/4}\,\psi_2^{1/2} + \zeta_2^{1/2}\,\psi_2}{\exp\left(\eta_2 + \zeta_2^{3/4}\,\psi_2^{1/2} + \frac{1}{2}\zeta_2^{1/2}\,\psi_2\right) - 1}, \\
D_{\rm BC}^{(3)} &= 3 - \frac{\left[(\lambda')^{2/3}\,\mu - (3\mu)^2\right]^{1/2} + \zeta_3^{2/3}\,\psi_3 + \frac{1}{2}\zeta_3^{1/2}\,\psi_3^{3/2}}{\exp\left\{\eta_3 + \left[(\lambda')^{2/3}\,\mu - (3\mu)^2\right]^{1/2} + \frac{1}{2}\zeta_3^{2/3}\,\psi_3 + \frac{1}{6}\zeta_3^{1/2}\,\psi_3^{3/2}\right\} - 1},
\end{aligned} \tag{57}$$

where we defined, for convenience,

$$\begin{aligned}
\delta_n &= \begin{cases} 2, & n = 1 \\ 8, & n = 2 \\ 48, & n = 3, \end{cases} \\
\zeta_n &= \frac{\delta_n}{\gamma_n}\eta_n \frac{\langle a\rangle^n}{\langle a^n\rangle}, \\
\psi_n &= \frac{1}{2}\delta_n^{1/n} - \zeta_n^{1/n}, \\
\lambda' &= \eta_3 \frac{[(3\pi)^2\langle a^2\rangle]^{3/2}}{\gamma_3\langle a^3\rangle}.
\end{aligned} \tag{58}$$

Here δ_n is a geometrical factor associated with the volume of an n-dimensional cube (or box). Note the similarity of $\zeta_n, \psi_n, \lambda'$ to ν_n, ϕ_n, λ, respectively, of the previous section.

The BC result for the one-dimensional case is identical to the MS result. This is due to the fact that in 1D both a box and a sphere reduce to a line segment. For $n = 2, 3$ the geometrical factors are different (γ_n for the MS and δ_n for BC). In Sec. III A 3 these issues will be considered in detail.

3. The distribution functions

In this section the effect of polydispersivity is examined explicitly, by assuming various functional forms for the radii distributions.

To assess the influence of polydispersivity we considered four types of common continuous distributions of radii, as well as a simple discrete bimodal distribution. These are compared for reference with the case of monodispersed radii treated for BC in Sec. II. The distributions considered are

$$\begin{aligned}
P_N(a) &= \frac{1}{\sqrt{2\pi}b} e^{-(a-\langle a\rangle)^2/2b^2} && \text{(normal)}, \\
P_U(a) &= \begin{cases} 1/b, & \langle a\rangle - \frac{1}{2}b \le a \le \langle a\rangle + \frac{1}{2}b \\ 0, & \text{else} \end{cases} && \text{(uniform)} \\
P_E(a) &= \frac{1}{\langle a\rangle} e^{-a/\langle a\rangle} && \text{(exponential [26])}, \\
P_S(a) &= \frac{1}{\Gamma(\langle a\rangle/b)} b^{-\langle a\rangle/b}\, a^{(\langle a\rangle - b)/b}\, e^{-a/b} && \text{(Schulz [27])}, \\
P_B(a) &= \begin{cases} \Pr[a = \langle a\rangle - (1-p)b] = p \\ \Pr[a = \langle a\rangle + p\,b] = 1 - p \end{cases} && \text{(bimodal)},
\end{aligned} \tag{59}$$

where b is in all cases a measure of the width of the distribution. A comparison of the distributions for two combinations

of $\langle a \rangle$ and b values is shown in Fig. 6, where they can be seen to differ significantly. In order to understand the difference between these distributions in the present context, note that $D_{\mathrm{BC}}^{(n)}$ and $D_{\mathrm{MS}}^{(n)}$ are determined by the first n moments of the distributions. Therefore it is useful to summarize the differences as follows: let $y_n = \langle a^n \rangle / \langle a \rangle^n$ and $z = b/\langle a \rangle$. Then

$$\begin{array}{lll} y_2 = 1+z^2, \quad y_3 = 1+3z^2 & & \text{(normal)} \\ y_2 = 1+\frac{z^2}{12}, \quad y_3 = 1+\frac{z^2}{4} & & \text{(uniform)} \\ y_2 = 2, \quad y_3 = 6 & & \text{(exponential)} \\ y_2 = 1+z, \quad y_3 = 1+3z+2z^2 & & \text{(Schulz)} \\ y_n = p[1-(1-p)z]^n + (1-p)(1+pz)^n & & \text{(bimodal).} \end{array} \tag{60}$$

However, the effect of assuming these different radii distributions on the MS and BC functions, and on the respective FD's is marginal in spite of the differences among them, as shown next.

B. Results

1. Range of linearity and the effect of dimensionality

In order to meaningfully compare the results in different dimensions, it is most convenient to fix the average distance $\langle x \rangle \equiv \rho^{-1/n}$ between sphere centers. Note that this implies different coverages, since from Eq. (51): $\eta_n = \gamma_n(\langle a \rangle / \langle x \rangle)^n$. In particular, since typically $\langle a \rangle \ll \langle x \rangle$, η_3 will be much smaller than η_1 for the same average distance. With this choice, a general estimate for the range of linearity, independent of the dimension, may be found. Suppose $\langle x \rangle = 10^k \langle a \rangle$; using the values for the cutoffs, $R_0 = \langle a \rangle$ and $R_1 = \frac{1}{2}\rho^{-1/n} - \langle a \rangle$, one has $\Delta_n \leq \log_{10} R_1 - \log_{10} R_0 = \log_{10}\left(\frac{1}{2}\langle x \rangle / \langle a \rangle - 1\right) = \log_{10}\left(\frac{1}{2}10^k - 1\right) \sim k - 0.3$ for $k > 1$. As discussed in Sec. II C 2, the range of linearity is limited both by the distance between cutoffs, which tends to increase when the coverage decreases, and by the quality of the linear regression, measured by $\mathcal{R}^2$, which tends to improve as the coverage increases. These trends are independent of the embedding space dimension and therefore in all dimensions we observe apparent fractality within a range of 1–2 orders of magnitude.

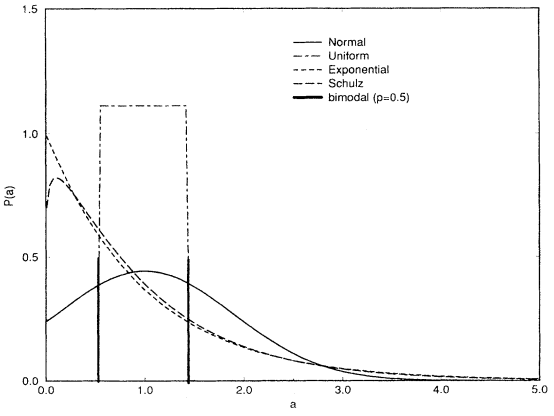

FIG. 6. Probability distributions $P(a)$ used for polydispersivity in radii of penetrable spheres model: Normal, uniform, exponential, Schulz, bimodal. All distributions have the same average $\langle a \rangle$ and width b, defined in the text. Shown here is the wide case, $\langle a \rangle = 1$, $b = 0.9$.

2. Comparison of box-counting and Minkowski-sausage results

It is comforting to find that, by and large, the BC and MS methods of resolution analysis yield very similar results. This is shown in Fig. 7, where the two meth-

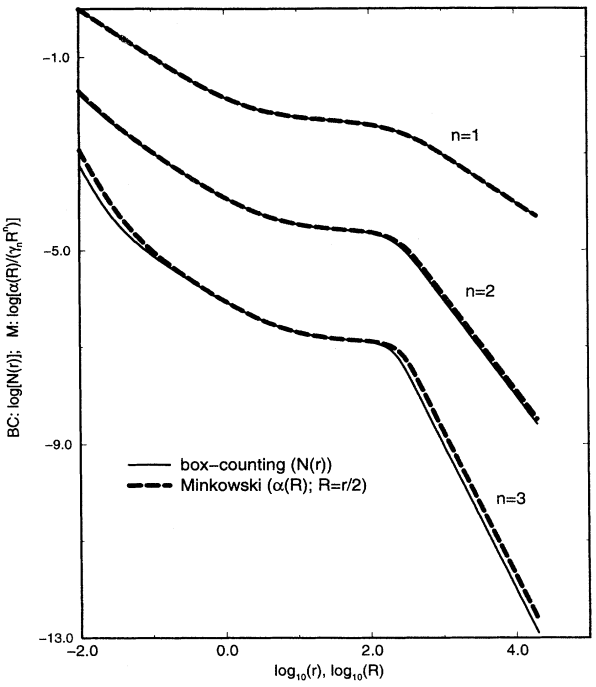

FIG. 7. Comparison of box-counting ($\log_{10}[N(r)]$ vs $\log_{10}(r)$) and Minkowski ($\log_{10}[\alpha(R)]$ vs $\log_{10}(R)$) functions for monodispersed, mutually penetrable spheres in $n = 1, 2, 3$ dimensions. The linear density is fixed at $\rho_1 = 0.05/a$, where $a = 1$ is the sphere radius. A meaningful comparison is achieved by plotting the Minkowski function normalized to the sphere volume ($\gamma_n R^n$), with $R = r/2$. In 1D BC and MS are identical. Differences do develop, albeit for ruler sizes (r, R) beyond the cutoffs, for $n = 2$ and $n = 3$, which depend on $\langle a^2 \rangle$ and $\langle a^2 \rangle, \langle a^3 \rangle$, respectively, and have different geometrical factors due to the use of boxes and M spheres. Note that $N(r)$ and $\alpha(R)$ are normalized to the total number of boxes and to the total volume, respectively.

ods are compared for the monodispersed case (quantitatively similar differences result for polydispersivity). When properly normalized (see caption), the methods are identical in 1D, and differ slightly in 2D and 3D. We shall see below that the FD values do not differ by more than 0.05 for 2D and 0.1 for 3D either, with MS giving the consistently lower values (see Figs. 10 and 11 below). We attribute the small variance between the two methods to the finite size of the basic building blocks, and to the differences in the geometrical factors γ_n and δ_n, which determine the details of lowering the resolution of observation. As the difference is so small, in the next section the entire discussion is held in terms of BC.

3. *Effect of polydispersivity on the BC function*

The BC function is displayed as a function of yardstick size in Figs. 8 and 9 for the distributions considered above, for a representative density of spheres, corresponding to an average intersphere distance $\langle x \rangle$ of 20 sphere radii (see captions for details). The average radius $\langle a \rangle$ and width b were set equal for all distributions. The value of $b = 0.9\langle a \rangle$ was chosen so as to reflect a very broad distribution. Values of b larger than $\langle a \rangle$ are not permissible since this would lead to negative radii. An observation of significant importance is that the qualitative (and to a large extent also the quantitative) nature of the results is unaffected by changing b. The BC function for the 1D case depends only on the average radius, as is clear from Eqs. (44) and (54), and hence no difference is observed between distributions with the same $\langle a \rangle$ in the 1D case. For 2D $\langle a^2 \rangle$ enters, which depends, in turn, on the specific distribution [Eq. (59)]. For 3D also $\langle a^3 \rangle$ enters, so that a stronger dependence on the distributions results. However, as seen in Figs. 8 and 9, the differences in BC function for different distributions set in only at small r values, close to the lower cutoff, and are always bounded.

The two most important questions in the context of apparent fractality relate to the slopes and the ranges of linearity. The former is dealt with in detail in the next subsection. As for the range of linearity of the scaling region, it appears that this is slightly decreased when polydispersivity is compared to monodispersivity.

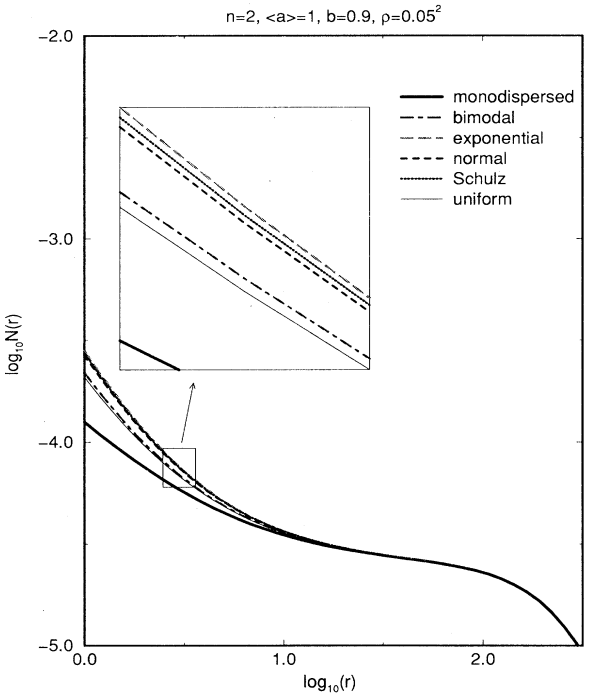

FIG. 8. BC functions for polydispersed, mutually penetrable spheres in $n = 2$ dimensions. As in Fig. 7, the linear density is $\rho_1 = 0.05/\langle a \rangle$ (note that ρ has dimensions of inverse area). The distribution parameters are $\langle a \rangle = 1$, $b = 0.9$. As seen clearly in the inset, the exponential distribution lies highest, followed by Schulz, normal, bimodal, uniform, and finally the monodispersed case (no distribution). Since the lower cutoff is expected at $\sim \log_{10} 1 = 0$, it appears that the effect of polydispersivity is to decrease the range of linearity somewhat.

4. *Effect of polydispersivity on fractal dimension*

The FD is displayed as a function of coverage in Figs. 10 and 11 for the distributions of Eq. (59). The average radius $\langle a \rangle$ and width b were set equal for all distributions, with $b = 0.9\langle a \rangle$ chosen again so as to reflect the unfavorable case of a very broad distribution (see

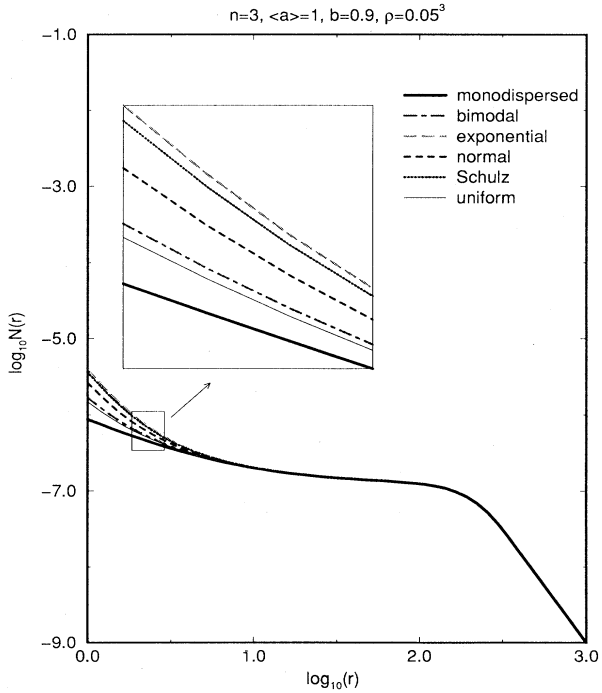

FIG. 9. Same as Fig. 8, but in $n = 3$ dimensions (ρ has dimensions of inverse volume). The asymmetry between the lower and upper cutoffs is apparent.

captions for details). Changing among distributions is seen to have only a minor effect on the FD, for the entire coverage range. A somewhat stronger effect is observed for 3D than for 2D. For 1D, as seen in Eqs. (50) and (57), the FD depends only on the average sphere radius (i.e., rod length), which was taken identical for all distributions, so that they necessarily all produce the same FD. However, the second and third moments $\langle a^2 \rangle$, $\langle a^3 \rangle$, which determine $D^{(2)}$ and $D^{(3)}$ through Eqs. (50) and (57), do depend on the particular distribution, and must affect, therefore, the FD. Comparing the moments of Eq. (60) reveals why the FD is so robust with respect to change of radius distribution or its parameters: recalling that $z < 1$ in order to assure positivity of the radii, observe that y_n are typically close to 1 (the monodispersed case) in all cases, except for the exponential distribution. (For the bimodal distribution it is straightforward to show that $0 < y_n < 1$ (recall that $0 < p < 1$), and is close to zero only for very small p and z.) However, even for the exponential distribution, it is seen in Figs. 10 and 11 that although the corresponding FD is indeed somewhat displaced, it is still very close to that of the other distributions. Thus, it is the combined effect of the relatively small dependence of the moments on the underlying radius distribution in the parameter range of interest, together with the even further suppressed sensitivity of the FD to these dependences, that is responsible for the robustness of the FD. The insensitivity of the model to polydispersivity is in support of our proposition that *the random adsorption model is generic: its features are virtually unaffected by (strong) perturbations in this commonly encountered way.*

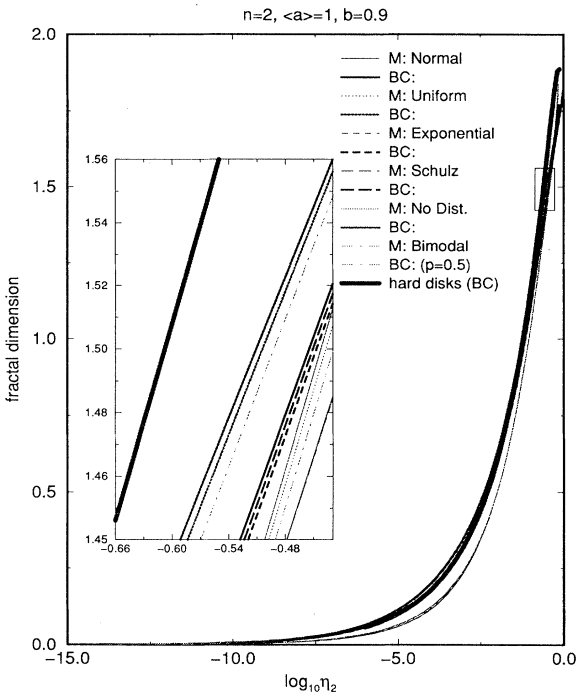

FIG. 10. Fractal dimension, obtained as slope of the BC and Minkowski functions at the estimated middle points r_e, R_e, for polydispersed, mutually penetrable spheres in 2D, as a function of the coverage, $\log_{10}\eta_2$. The minimal coverage is as in Fig. 5. Displayed here are the broad distribution results: $\langle a \rangle = 1$, $b = 0.9\langle a \rangle$. Small differences are observed among the distributions. The order is opposite to that in Fig. 7, with the Minkowski dimension consistently somewhat smaller. Also shown is the FD for impenetrable disks, which as expected, is slightly larger. The lowest coverage shown corresponds to the lowest molecular densities observed in nature: 10 Å/cm^3 in intergalactic space.

IV. SOLUTION OF THE IMPENETRABLE SPHERES CASE

A. The model

Consider now a different model, which adds correlations on top of the model of equisized, mutually penetrable spheres by imposing impenetrability on a system of n-dimensional spheres at equilibrium [28]. Impenetrability creates a negative correlation in sphere positions. This model is fully solvable for $n = 1$, and approximately solvable with high accuracy for $n = 2, 3$. It represents an important class of processes with correlations, such as models of hard-sphere liquids, energy-level repulsion in quantum systems that are classically chaotic [19], Langmuir-type adsorption, etc. As demonstrated below, the correlation due to impenetrability merely *modifies* the apparent fractal character already induced by the

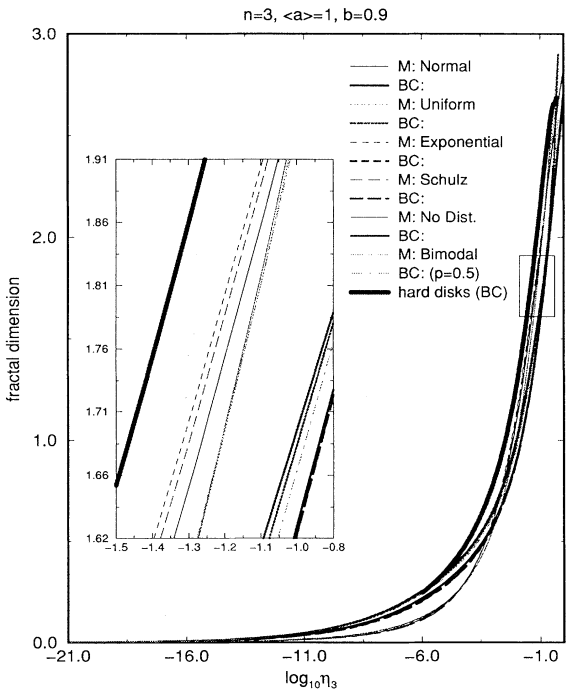

FIG. 11. Fractal dimension, obtained as slope of the BC and Minkowski function in 3D. The details are the same as in Fig. 10 and the results are qualitatively the same as in 2D.

random nature of the problem. We limit ourselves to a BC analysis of this problem.

B. Derivations for 1D case

Consider first the 1D case of impenetrable rods: the BC function is calculated by employing a result derived using thermodynamic arguments by Helfand, Frisch, and Lebowitz [29], and using a statistical argument by Torquato, Lu, and Rubinstein [30]. They show that the probability of finding a cavity of length l containing no rod centers, in a system of a large number of impenetrable rods of length d each, is

$$q^{(1)} = (1-\eta_1)\exp\left[\frac{-\eta_1}{(1-\eta_1)}\left(\frac{l}{d}-1\right)\right] \tag{61}$$

for $l > d$. In performing BC, for a box of length r to remain empty, no rod center may fall within $d/2$ from either side of the box, so that $l = r + d$. $q^{(1)}$ may be rewritten, in the limit of a large number of rods ($M \to \infty$ at fixed coverage), as

$$\begin{aligned} q^{(1)} &= (1-\eta_1)\left[1-\left(\frac{l}{d}-1\right)\frac{\eta_1}{1-\eta_1}\frac{1}{M}\right]^M \\ &= (1-\eta_1)\left(1-\frac{r}{1-\eta_1}\right)^M . \end{aligned} \tag{62}$$

Having $p = 1 - q$ and using Eq. (5) the expected number of intersected boxes is

$$\langle N(r)\rangle = \frac{1}{r}\left[1-(1-\eta_1)\left(1-\frac{r}{1-\eta_1}\right)^M\right]. \tag{63}$$

As in the penetrable rods case, one can now use Eq. (2) (with the slope calculated at $r = r_e$) to calculate a lower bound for the FD. We obtain

$$\begin{aligned} D = 1 &- \eta_1\sqrt{\frac{1}{\eta_1}-1} \\ &\times \frac{[1-\sqrt{\eta_1/(1-\eta_1)}/M]^{M-1}}{1-(1-\eta_1)\left[1-\sqrt{\eta_1/(1-\eta_1)}/M\right]^M}. \end{aligned} \tag{64}$$

This can again be simplified for large M:

$$D = 1 - \frac{\eta_1\sqrt{1/\eta_1-1}}{\exp\left[\sqrt{\eta_1/(1-\eta_1)}\right]-(1-\eta_1)}. \tag{65}$$

C. Derivations for 2D and 3D cases

So far all the results were based on exact calculations. We now consider an approximate solution for 2D and 3D impenetrable spheres. Full analytical solutions are at present impossible: exact results for the probability of finding a cavity containing no disk or ball centers after their placement, as employed in Eq. (61) above, are not available because the n-particle probability densities are not exactly known. Nevertheless, Refs. [30,31] provide some accurate approximations for the probability of finding a two- or three-dimensional spherical cavity of radius l in an equilibrium system of hard spheres of radius a.

1. BC function

In the context of BC, one in fact requires the probability of finding a cavity with the shape of the convolution of a box and sphere [see Sec. II and Fig. 1(c)]. This will be undertaken in a future study; at present we will settle for an approximation of the cavity by spheres. The important quantity to conserve in this approximation is the cavity volume, since this is what actually enters the probabilistic argument at the root of the calculation of the BC function. If one simply takes the spherical cavity radius as the geometric mean of the sphere radius plus half box length, and sphere radius plus half box diagonal,

$$l_n(r) = \left[\left(\frac{r}{2}+a\right)\left(\frac{1}{2}\sqrt{n}+a\right)\right]^{1/2}, \tag{66}$$

the real cavity volume [see Eqs. (9) and (11)] is overestimated by no more than 10% in 2D, and (except for a sharp maximum of 80% for $0.2 < r/a < 5$) by no more than 20% in 3D. This will suffice for the present purpose of an approximate treatment of the 2D and 3D impenetrable spheres problem. Now, the results of Ref. [30] for the empty-cavity probability in n dimensions can be expressed conveniently as follows:

$$q^{(n)}(r) = (1-\eta_n)\exp\left(\frac{-\eta_n}{(1-\eta_n)^n}f_n(r)\right), \tag{67}$$

where the subscript n on the coverage η serves to remind that the same coverage defines different combinations of sphere sizes and densities for different dimensions [see Eq. (51) in the monodispersed case]. The functions f_n depend on the particular approximation used, but have the general form

$$f_n(r) = \sum_{j=0}^{n}\alpha_j^{(n)}(\eta_n)\,x_n^j; \qquad x_n = \frac{l_n(r)}{2a}. \tag{68}$$

The $\alpha_j^{(n)}$ are, for $n = 2$ (impenetrable disks), using the scaled-particle theory of Reiss, Frisch and Lebowitz [32]:

$$\alpha_0^{(2)} = 2\eta - 1, \quad \alpha_1^{(2)} = -4\eta, \quad \alpha_2^{(2)} = 4, \tag{69}$$

whereas for $n = 3$, using the Carnahan-Starling result [33], Ref. [30] finds

$$\alpha_0^{(3)} = -\frac{1}{2}(9\eta^2 - 7\eta + 2), \quad \alpha_1^{(3)} = 12\eta^2,$$
$$\alpha_2^{(3)} = -6\eta(3+\eta), \quad \alpha_3^{(3)} = 8(1+\eta). \tag{70}$$

Next, the BC functions are given, as usual, by

$$\langle N^{(n)}(r)\rangle = \frac{1}{r^n}\left(1 - q^{(n)}\right). \tag{71}$$

The apparent FD's predicted by these results are discussed next.

2. Fractal dimension

For the 2D and 3D cases, the FD is obtained by evaluating the logarithmic derivative at $r_e^{(n)} = \left[2a\left(\rho^{-1/n} - 2a\right)\right]^{1/2}$. Using Eq. (51), the estimated middle point of the scaling range can be rewritten as

$$\frac{r_e^{(n)}}{a} = 2h_n(\eta), \quad h_n(\eta) = \left[\frac{1}{2}\left(\frac{\gamma_n}{\eta_n}\right)^{1/n} - 1\right]^{1/2}. \tag{72}$$

The hard-sphere radius a cancels out and the FD for $n = 2, 3$ is found to be given by

$$D^{(n)} = \left.\frac{d(\log_{10}[N^{(n)}(r)])}{d(\log_{10}[1/r])}\right|_{r=r_e} = n - \frac{1}{2}\frac{\eta_n}{(1-\eta_n)^{n-1}} h_n(\eta_n)[\sqrt{n}(2h_n(\eta_n)+1)+1]$$
$$\times \frac{\sum_{j=1}^{n} 2^{-j}\alpha_j^{(n)}(\eta_n)\, j\, \{[1+h_n(\eta_n)][1+\sqrt{n}h_n(\eta_n)]\}^{j/2-1}}{\exp\left[[\eta_n/(1-\eta_n)^n]\sum_{j=0}^{n} 2^{-j}\alpha_j^{(n)}(\eta_n)\{[1+h_n(\eta_n)][1+\sqrt{n}h_n(\eta_n)]\}^{j/2}\right] - (1-\eta_n)}. \tag{73}$$

It should be noted that $D^{(n)}$ are functions of η_n alone, which indeed, in contrast to the penetrable spheres case, is exactly the volume fraction of space occupied by the impenetrable spheres.

D. Results

1. Effect of impenetrability on the BC function and on the range of linearity

Figure 12 shows the plot of Eq. (8) for the penetrable rods case, together with the expression for $\langle N(r)\rangle$ in the 1D impenetrable rods case, Eq. (63). The behavior is qualitatively similar in both cases, and virtually indistinguishable for low coverages. Figure 12 thus *demonstrates the primary role of pure randomness in the appearance of fractality, even in the presence of correlations*, at least at coverages below 10%.

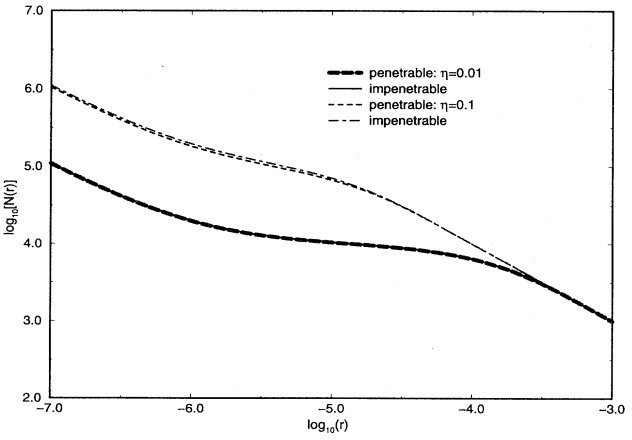

FIG. 12. Comparison of box-counting predictions in penetrable and impenetrable rods cases. The results for penetrable [Eq. (8)] and impenetrable rods [Eq. (63)] virtually coincide for $\eta \leq 10^{-2}$. For $\eta = 0.1$ a barely noticeable difference develops. $d = 10^{-6}$ in both cases.

The impenetrability case results for 2D and 3D are shown in Figs. 10 and 11, respectively, along with those for penetrable spheres. As in the 1D case, the effect of impenetrability is virtually unnoticeable in terms of the FD. Once more, it appears that *the scaling content of this highly nontrivial system is already contained to a very large extent in its penetrable counterpart.*

2. Effect of impenetrability on fractal dimension

The result for 1D is shown in Fig. 5. As expected, the FD rises to 1 faster than in the penetrable rods case: when no overlap is allowed, the line is filled up at lower coverages. The important observation is the large range of coverages for which the penetrable and impenetrable rods FD's nearly overlap. For all practical purposes, therefore, the FD is very close in these two cases, which differ significantly in the extent of correlations present in the respective systems: the fractal content of the impenetrable rods geometry is already contained to a large extent in the associated random penetrable rods case.

V. CONCLUSIONS

We have shown in this paper that randomness in its most elementary forms generates apparent fractal structures over 1–2 decades, between a lower cutoff—the elementary building block—and an upper cutoff, which is approximately the average distance between building

blocks. We adopted an empirical-like approach to the calculation of fractal dimension: we deliberately considered sets bound within natural finite cutoffs, which display scaling behavior over *a physically relevant range*. We believe this approach to be both useful and necessary, if a direct contact between theory and experiment is to be achieved. This led us to consider several simple, but widely applicable models of random phenomena, with and without correlations, obtaining as one of the main results, an analytical solution for the apparent fractal dimension of models of randomness. The models studied are convenient starting points for other, more elaborate ones of random phenomena. It is argued that the models we have studied are, in fact, prototypical of a large class of spatial, temporal, and even spectral random phenomena. The methods introduced here should be useful in the study of further cases of random phenomena, with other types of disorder and correlations. To conclude, we would like to point out that apparent fractal behavior is expected to occur for a more general class of distributions. Generally, the $\log_{10}N(r)$ versus $\log_{10}(1/r)$ plot includes lines of slope $D = n$ $(n = 1, 2, 3)$ beyond the upper and lower cutoffs, which are connected by an interval of slope $D < n$, which depends on the specific distribution.

ACKNOWLEDGMENTS

We would like to thank P. Bak, R.B. Gerber, C. Jayaprakash, D. Mukamel, J. Sethna, and G. Shinar for very helpful discussions.

[1] B. B. Mandelbrot, *The Fractal Geometry of Nature* (Freeman, San Francisco, 1982).

[2] *Fractals in Physics, Essays in Honour of B.B. Mandelbrot*, edited by J. Feder and A. Aharony (North-Holland, Amsterdam, 1990).

[3] *Fractals in Science*, edited by A. Bunde and S. Havlin (Springer, Berlin, 1994).

[4] *On Growth and Form*, Vol. 100 of *NATO Advanced Studies Institute Series E: Applied Sciences*, edited by H. E. Stanley and N. Ostrowsky (Martinus Nijhoff, Dordrecht, 1986).

[5] *The Fractal Approach to Heterogeneous Chemistry: Surfaces, Colloids, Polymers*, edited by D. Avnir (Wiley, Chichester, 1992).

[6] H. Takayasu, *Fractals in the Physical Sciences* (Wiley, Chichester, 1990).

[7] *Scaling Phenomena in Disordered Systems*, Vol. 133 of *NATO Advanced Studies Insitute Series B: Physics*, edited by R. Pynn and A. Shjeltrop (Plenum, New York, 1985).

[8] P.-G. de Gennes, *Scaling Concepts in Polymer Physics* (Cornell University Press, Ithaca, 1979).

[9] A.-L. Barabási and H.E. Stanley, *Fractal Concepts in Surface Growth* (Cambridge University Press, Cambridge, 1995).

[10] D.A. Hamburger, O. Biham, and D. Avnir (unpublished).

[11] K. Falconer, *Fractal Geometry: Mathematical Foundations and Applications* (Wiley, Chichester, 1990).

[12] For a line of length L, normalize all lengths to L.

[13] H.L. Weissberg, J. Appl. Phys. **34**, 2636 (1963).

[14] S. Torquato and G. Stell, J. Chem. Phys. **79**, 1505 (1983).

[15] In Ref. [10], we include a histogram, based on all the experimental FD measurements presented in Ref. [2], and showing the number of plots as a function of the number of decades of the linear range. The conclusion is that by and large, most experimental measurements of fractal dimensions are based on data that extends between one and two decades.

[16] P. Pfeifer and M. Obert, in *The Fractal Approach to Heterogeneous Chemistry: Surfaces, Colloids, Polymers*, edited by D. Avnir (Wiley, Chichester, 1992), pp. 38–39.

[17] P. Meakin and J.M. Deutch, J. Chem. Phys. **83**, 4086 (1985).

[18] L.S. Cederbaum, E. Haller, and P. Pfeifer, Phys. Rev. A **31**, 1869 (1985).

[19] M.V. Berry and M. Tabor, Proc. R. Soc. London A **356**, 375 (1977).

[20] F.M. Reza, *An Introduction to Information Theory* (McGraw-Hill, New York, 1961).

[21] K.A. Brownlee, *Statistical Theory and Methodology* (Wiley, New York, 1965), p. 169.

[22] H. Röder, E. Hahn, H. Brune, J.-P. Bucher, and K. Kern, Nature **366**, 141 (1993).

[23] H. Brune, C. Romainczyk, H. Röder, and K. Kern, Nature **369**, 469 (1994).

[24] G. Rosenfeld, A.F. Becker, B. Poelsema, L.K. Verheij, and G. Comsa, Phys. Rev. Lett. **69**, 917 (1992).

[25] η_n is an appropriate variable in the context of sequential addition of n-dimensional spheres, such as in an adsorption experiment. When one is *a priori* faced with the final result of overlapping spheres, such as in random spectra or the distribution of craters on an asteroid [M. J. S. Belton *et al.*, Science **265**, 1543 (1994)], it is more convenient to work with the *net* coverage, $\alpha^{(n)}(0) = 1 - \exp(\eta_n)$, of Eq. (44).

[26] A nearly exponential distribution of relatively compact (i.e., circular) clusters was found in embedded-atom simulations of Ag on Pt(111) [P. Blandin, C. Massobrio, and P. Ballone, Phys. Rev. Lett. **72**, 3072 (1994)].

[27] The Schulz distribution is a continuous version of the discrete Gamma distribution. Its standard formula is $P_S(a) = \frac{1}{\Gamma(m+1)}\left(\frac{m+1}{\langle a\rangle}\right)^{m+1} a^m\, e^{-(m+1)a/\langle a\rangle}$ [G. V. Schulz, Z. Phys. Chem. B **43**, 25 (1939)], where $m > -1$ determines the peakedness of the distribution. A general expression for the nth moment is $\langle a^n\rangle = b^n \prod_{i=1}^{n}\left(\frac{a-b}{b} + i\right)$. The parameter b we introduced is a measure of the width of the distribution: $b = \langle a\rangle - a^*$,

where $a^* = \langle a \rangle \frac{m}{m+1}$ is the position of the maximum of $P_S(a)$.

[28] Equilibrium and nonequilibrium distributions such as random sequential adsorption are known to be different at the same coverage; see B. Widom, J. Chem. Phys. **44**, 3888 (1966).

[29] E. Helfand, H.L. Frisch, and J.L. Lebowitz, J. Chem. Phys. **34**, 1037 (1961).

[30] S. Torquato, B. Lu, and J. Rubinstein, Phys. Rev. A **41**, 2059 (1990).

[31] S. Torquato and S.B. Lee, Physica A **167**, 361 (1990).

[32] H. Reiss, H.L. Frisch, and J.L. Lebowitz, J. Chem. Phys. **31**, 369 (1959).

[33] N.F. Carnahan and K.E. Starling, J. Chem. Phys. **51**, 635 (1969).